Core breaking and possible magnetic rotation in the semimagic nucleus ^{90}Zr*

Hao Wang(王豪)[1] Ke-Yan Ma(马克岩)[1†] Si-Ying Liu(刘斯颖)[1] Jing-Bin Lu(陆景彬)[1‡]

[1]College of Physics, Jilin University, Changchun 130012, China

Abstract: The semimagic nucleus ^{90}Zr, with $Z = 40$ and $N = 50$, is investigated in terms of large scale shell model calculations. A logical agreement is obtained between the available experimental data and predicted values. The calculated results indicate that the low-lying states are primarily dominated by the proton excitations from the *fp* orbitals across the $Z = 38$ or 40 subshell into the high-j $1g_{9/2}$ orbital. For the higher-spin states of ^{90}Zr, the breaking of the $N = 50$ core plays a crucial role, and the contribution of different orbitals to each state are discussed in this article. The evolution from neutron core excitations to proton excitations is systematically studied along the neighboring $N = 50$ isotones. Furthermore, the strong $\Delta I = 1$ sequence demonstrates an abrupt backbend attributed to the alignment of the valence nucleons in *fp* proton orbitals and is proposed to have a $\pi(fp)^{-2}(1g_{9/2})^2 \otimes \nu(1g_{9/2})^{-1}(2d_{5/2}/1g_{7/2})^1$ configuration before the backbend, based on the shell model calculations. The properties of this sequence before the backbend indicate a general agreement with the fingerprints of magnetic rotation; hence, the sequence with the $\pi(fp)^{-2}(1g_{9/2})^2 \otimes \nu(1g_{9/2})^{-1}(2d_{5/2}/1g_{7/2})^1$ configuration is suggested as a magnetic rotational band arising from shears mechanism.

Keywords: semimagic nucleus, shell model, core breaking, magnetic rotation

DOI: 10.1088/1674-1137/ac0fd2

I. INTRODUCTION

The study on level structures is significantly interesting in weakly deformed and nearly spherical nuclei [1-9]. In particular, the nuclei with $N \sim 50$ in the $A \sim 90$ mass region provide a suitable laboratory to study the mechanism of particle-hole excitations. The low-lying states of these nuclei are well described within the shell model framework, mainly exhibiting the characteristics of single-particle excitations [5-10]. With an increase in the excitation energy, the medium spin states are predominated by the multi-quasiparticle excitations outside the inert core. As the energy and spin further increase, the higher-spin states could be dominated by the excitation of the neutron across the $N = 50$ core into the next major shell, such as the breaking of the $N = 50$ core. This phenomenon a critical topic in the $A \sim 90$ mass region, and has been reported systematically in the $N = 50$ isotones [6-22]. However, the relevant research for ^{90}Zr nucleus with $N = 50$ is relatively insufficient [23-26], and earlier studies on this nucleus mainly focus on lower-spin states. Hence, it is necessary to further investigate level structures and explore possible neutron core excitations in a semimagic nucleus ^{90}Zr, using the large scale shell model calculations. Accordingly, the evolution from the neutron core excitations to proton excitations across the $Z = 38$ or 40 subshell along the $N = 50$ isotones (^{85}Br, ^{86}Kr, ^{87}Rb, ^{88}Sr, ^{89}Y, ^{90}Zr, ^{91}Nb, ^{92}Mo, ^{93}Tc, ^{94}Ru) is systematically discussed in the present work.

In addition, the magnetic rotation is another significantly interesting topic in our current study. It can be sufficiently interpreted by the tilted axis cranking covariant density functional theory (TAC-CDFT) [27-30]. In addition, semiclassical calculations can also provide a logical description for the shears mechanism [31-34]. In the $A \sim 90$ mass region, many magnetic rotational bands have been reported in Br, Kr, Rb, and Sr nuclei [35-42], which are strong $\Delta I = 1$ bands based on the high-j particle-hole configurations. Interestingly, a similar structure also emerges in the ^{90}Zr nucleus, and a detailed discussion on this structure is presented in Sec. IIIC.

Received 11 April 2021; Accepted 30 June 2021; Published online 30 July 2021

* Supported by the National Natural Science Foundation of China (11775098, U1867210, 11405072), Jilin Scientific and Technological Development Programs (20190201137JC, 20180520195JH), the 13th Five-Year Plan of Scientific Research of Jilin Province (JJKH20180117KJ), China Postdoctoral Science Foundation (2015M571354, 2013M541285), the Fundamental Research Funds for the Central Universities, and the Graduate Innovation Fund of Jilin University

† E-mail: mky@jlu.edu.cn

‡ E-mail: ljb@jlu.edu.cn

II. SHELL MODEL CALCULATIONS

The level structures of ^{90}Zr are investigated via large scale shell model calculations with the NUSHELLX code [43]. The GWB model space and GWBXG interaction are adopted in the code. The model space comprises four proton orbitals ($1f_{5/2}$, $2p_{3/2}$, $2p_{1/2}$, $1g_{9/2}$) and six neutron orbitals ($2p_{1/2}$, $1g_{9/2}$, $1g_{7/2}$, $2d_{5/2}$, $2d_{3/2}$, $3s_{1/2}$) relative to an inert ^{66}Ni ($Z = 28$, $N = 38$) core. The single-particle energies relative to the ^{66}Ni core are set as $\varepsilon^{\pi}_{1f_{5/2}} = -5.322$ MeV, $\varepsilon^{\pi}_{2p_{3/2}} = -6.144$ MeV, $\varepsilon^{\pi}_{2p_{1/2}} = -3.941$ MeV, $\varepsilon^{\pi}_{1g_{9/2}} = -1.250$ MeV, $\varepsilon^{\nu}_{2p_{1/2}} = -0.696$ MeV, $\varepsilon^{\nu}_{1g_{9/2}} = -2.597$ MeV, $\varepsilon^{\nu}_{1g_{7/2}} = 5.159$ MeV, $\varepsilon^{\nu}_{2d_{5/2}} = 1.830$ MeV, $\varepsilon^{\nu}_{2d_{3/2}} = 4.261$ MeV, and $\varepsilon^{\nu}_{3s_{1/2}} = 1.741$ MeV. These single-particle energies and the corresponding values of the strengths of the residual interactions are adopted to calculate level energies and provide an optimal description of the spectra for nuclei with $N \sim 50$ in the $A \sim 90$ mass region [7-9, 44].

III. DISCUSSION

The semimagic nucleus ^{90}Zr has 12 valence protons and 12 valence neutrons in the configuration space. Considering the large dimensionality of the matrices involved, truncations are employed to make the calculations feasible. In this study, two sets of shell model calculations (SM1 and SM2) are performed. For the SM1 configuration space, no neutron excitation is allowed across the $N = 50$ magic core, and the valence protons are redistributed in the $1f_{5/2}$, $2p_{3/2}$, $2p_{1/2}$, and $1g_{9/2}$ single-particle orbitals. SM2 adopts the same proton configuration space as SM1, and the influence of neutron core excitation $\nu(1g_{9/2})^{-1}(2d_{5/2}/1g_{7/2})^{1}$ is considered, i.e., one neutron is allowed from the completed filled $1g_{9/2}$ orbital across the $N = 50$ core into the $2d_{5/2}$ or $1g_{7/2}$ orbitals.

A. Proton excitations and neutron core breaking

The level scheme of ^{90}Zr deduced from Ref. [23] and the results of the shell model calculations (SM1 and SM2) are compared in Fig. 1. The main partitions of the wave function for each state within SM1 and SM2 are summarized in Table 1.

It can be seen from Fig. 1 that the 2^+_1, 4^+_1, 6^+_1, and 8^+_1 states are well reproduced in both SM1 and SM2. As

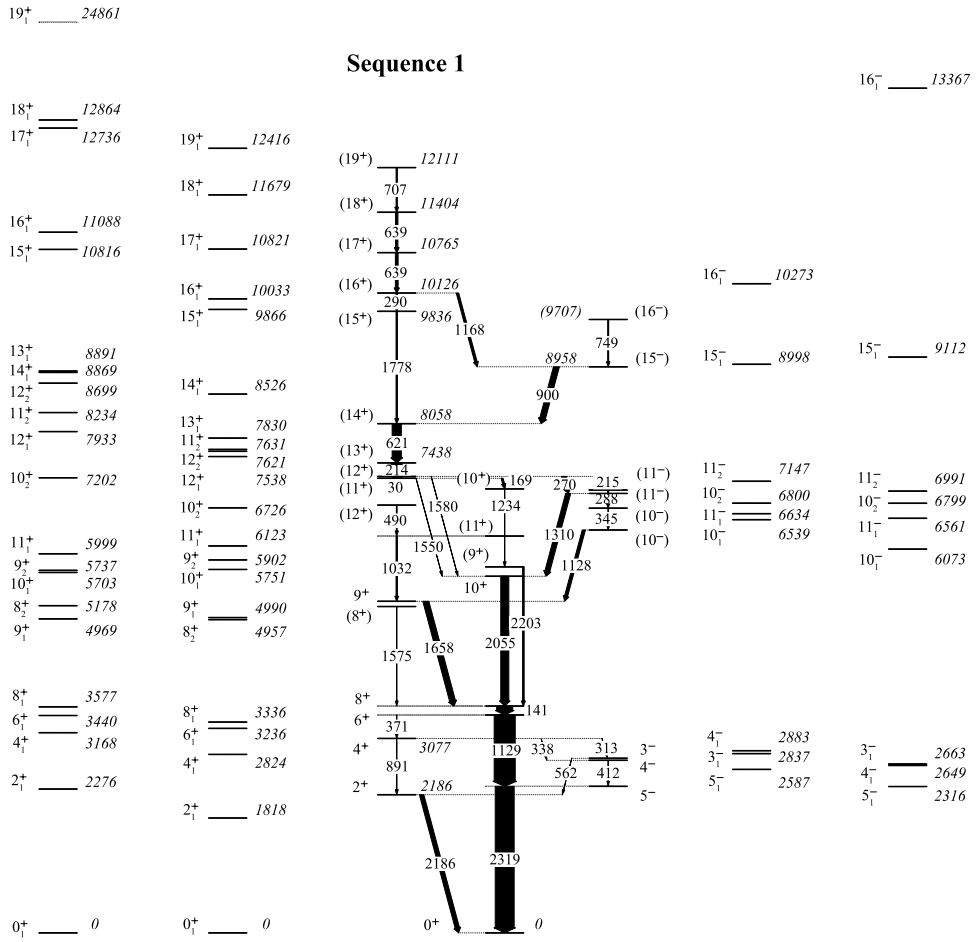

Fig. 1. Level scheme of ^{90}Zr deduced from Ref. [23], compared with the results obtained from the shell model calculations (SM1 and SM2).

Table 1. Main partitions of the wave functions for ^{90}Zr with SM1 and SM2 configuration spaces. The wave function for a particular angular momentum state would contain several partitions. Each partition is of the form $P=\pi[p(1), p(2), p(3), p(4)]\otimes\nu[n(1), n(2), n(3), n(4)]$, where $p(i)$ represents the number of valence protons occupying the $1f_{5/2}$, $2p_{3/2}$, $2p_{1/2}$, and $1g_{9/2}$ orbitals, and $n(j)$ represents the number of valence neutrons in the $2p_{1/2}$, $1g_{9/2}$, $1g_{7/2}$, and $2d_{5/2}$ orbitals.

$I^{\pi}(\hbar)$	$E_{(\mathrm{exp.})}$/keV	SM1				SM2			
		$E_{(\mathrm{cal.})}$/keV	Wave function $\pi\otimes\nu$	Seniority v	Partitions (%)	$E_{(\mathrm{cal.})}$/keV	Wave function $\pi\otimes\nu$	Seniority v	Partitions (%)
0_1^+	0	0	6 4 2 0 ⊗ 2 10 0 0	0	45.25	0	6 4 2 0 ⊗ 2 10 0 0	0	30.26
			6 4 0 2 ⊗ 2 10 0 0	0	22.45		6 4 0 2 ⊗ 2 10 0 0	0	20.89
2_1^+	2186	2276	6 4 0 2 ⊗ 2 10 0 0	2	50.68	1818	6 4 0 2 ⊗ 2 10 0 0	2	36.62
			4 4 2 2 ⊗ 2 10 0 0	2	16.21		4 4 2 2 ⊗ 2 10 0 0	2	16.69
4_1^+	3077	3168	6 4 0 2 ⊗ 2 10 0 0	2	54.83	2824	6 4 0 2 ⊗ 2 10 0 0	2	40.93
			4 4 2 2 ⊗ 2 10 0 0	2	14.36		4 4 2 2 ⊗ 2 10 0 0	2	15.55
6_1^+	3448	3440	6 4 0 2 ⊗ 2 10 0 0	2	59.52	3236	6 4 0 2 ⊗ 2 10 0 0	2	48.94
			4 4 2 2 ⊗ 2 10 0 0	2	12.43		4 4 2 2 ⊗ 2 10 0 0	2	14.05
8_1^+	3589	3577	6 4 0 2 ⊗ 2 10 0 0	2	63.07	3336	6 4 0 2 ⊗ 2 10 0 0	2	50.65
			4 4 2 2 ⊗ 2 10 0 0	2	12.07		4 4 2 2 ⊗ 2 10 0 0	2	13.48
8_2^+	5164	5178	5 4 1 2 ⊗ 2 10 0 0	2	47.53	4957	5 4 1 2 ⊗ 2 10 0 0	4	40.82
			5 3 2 2 ⊗ 2 10 0 0	2	25.20		6 3 1 2 ⊗ 2 10 0 0	4	19.89
9_1^+	5247	4969	5 4 1 2 ⊗ 2 10 0 0	4	73.08	4990	5 4 1 2 ⊗ 2 10 0 0	4	66.91
			5 3 2 2 ⊗ 2 10 0 0	4	11.91		5 3 2 2 ⊗ 2 10 0 0	4	10.64
9_2^+	5792	5737	6 3 1 2 ⊗ 2 10 0 0	4	67.49	5902	5 4 1 2 ⊗ 2 10 0 0	4	44.86
			5 4 1 2 ⊗ 2 10 0 0	4	13.93		6 3 1 2 ⊗ 2 10 0 0	4	21.38
10_1^+	5644	5703	5 4 1 2 ⊗ 2 10 0 0	4	76.91	5751	6 3 1 2 ⊗ 2 10 0 0	4	38.86
			5 3 2 2 ⊗ 2 10 0 0	4	13.72		5 4 1 2 ⊗ 2 10 0 0	4	20.99
10_2^+	7026	7202	4 4 0 4 ⊗ 2 10 0 0	4	55.80	6726	4 4 0 4 ⊗ 2 10 0 0	4	48.21
			4 4 2 2 ⊗ 2 10 0 0	4	8.65		4 3 1 4 ⊗ 2 10 0 0	4	7.85
11_1^+	6280	5999	5 4 1 2 ⊗ 2 10 0 0	4	73.52	6123	5 4 1 2 ⊗ 2 10 0 0	4	65.31
			5 3 2 2 ⊗ 2 10 0 0	4	14.18		5 3 2 2 ⊗ 2 10 0 0	4	12.46
11_2^+	7194	8234	4 4 0 4 ⊗ 2 10 0 0	4	34.60	7631	6 4 0 2 ⊗ 2 9 0 1	4	34.74
			5 3 0 4 ⊗ 2 10 0 0	4	24.19		4 4 2 2 ⊗ 2 9 0 1	4	16.23
12_1^+	6770	7933	4 4 0 4 ⊗ 2 10 0 0	4	62.69	7538	4 4 0 4 ⊗ 2 10 0 0	4	51.58
			4 3 1 4 ⊗ 2 10 0 0	6	12.98		4 3 1 4 ⊗ 2 10 0 0	6	10.90
12_2^+	7224	8699	5 3 0 4 ⊗ 2 10 0 0	4	29.17	7621	6 4 0 2 ⊗ 2 9 0 1	4	38.10
			4 4 0 4 ⊗ 2 10 0 0	4	26.84		4 4 2 2 ⊗ 2 9 0 1	4	17.05
13_1^+	7438	8891	5 3 0 4 ⊗ 2 10 0 0	6	38.03	7830	6 4 0 2 ⊗ 2 9 0 1	4	42.29
			4 4 0 4 ⊗ 2 10 0 0	6	33.83		4 4 2 2 ⊗ 2 9 0 1	4	17.69
14_1^+	8058	8869	4 4 0 4 ⊗ 2 10 0 0	6	70.98	8526	6 4 0 2 ⊗ 2 9 0 1	4	40.74
			4 3 1 4 ⊗ 2 10 0 0	6	22.62		4 4 2 2 ⊗ 2 9 0 1	4	14.72
15_1^+	9836	10816	5 3 0 4 ⊗ 2 10 0 0	6	29.71	9866	5 4 1 2 ⊗ 2 9 0 1	6	54.25
			5 2 1 4 ⊗ 2 10 0 0	6	22.90		4 4 2 2 ⊗ 2 9 0 1	6	7.32
16_1^+	10126	11088	5 3 0 4 ⊗ 2 10 0 0	6	38.12	10033	5 4 1 2 ⊗ 2 9 0 1	6	73.92
			5 2 1 4 ⊗ 2 10 0 0	8	27.82		5 3 2 2 ⊗ 2 9 0 1	6	13.27
17_1^+	10765	12736	3 4 1 4 ⊗ 2 10 0 0	8	53.79	10821	5 4 1 2 ⊗ 2 9 0 1	6	66.57
			4 3 1 4 ⊗ 2 10 0 0	8	32.73		5 3 2 2 ⊗ 2 9 0 1	6	14.64

Continued on next page

Table 1-continued from previous page

$I^{\pi}(\hbar)$	$E_{(\mathrm{exp.})}$/keV	SM1				SM2			
		$E_{(\mathrm{cal.})}$/keV	Wave function $\pi\otimes\nu$	Seniority ν	Partitions (%)	$E_{(\mathrm{cal.})}$/keV	Wave function $\pi\otimes\nu$	Seniority ν	Partitions (%)
18_1^+	11404	12864	4 3 1 4 ⊗ 2 10 0 0	8	81.57	11679	5 4 1 2 ⊗ 2 9 0 1	6	65.78
			4 2 2 4 ⊗ 2 10 0 0	8	17.73		5 3 2 2 ⊗ 2 9 0 1	6	12.87
19_1^+	12111	24861	3 2 1 6 ⊗ 2 10 0 0	10	100	12416	5 4 1 2 ⊗ 2 9 1 0	6	68.21
							5 3 2 2 ⊗ 2 9 1 0	6	12.66
3_1^-	2748	2663	6 3 2 1 ⊗ 2 10 0 0	2	71.33	2837	6 3 2 1 ⊗ 2 10 0 0	2	54.93
			6 3 0 3 ⊗ 2 10 0 0	2	7.63		6 3 0 3 ⊗ 2 10 0 0	2	13.05
4_1^-	2739	2649	6 4 1 1 ⊗ 2 10 0 0	2	79.08	2883	6 4 1 1 ⊗ 2 10 0 0	2	70.69
			6 2 1 3 ⊗ 2 10 0 0	2	10.19		6 2 1 3 ⊗ 2 10 0 0	2	10.68
5_1^-	2319	2316	6 4 1 1 ⊗ 2 10 0 0	2	79.03	2587	6 4 1 1 ⊗ 2 10 0 0	2	72.94
			6 2 1 3 ⊗ 2 10 0 0	2	9.54		6 2 1 3 ⊗ 2 10 0 0	2	10.42
10_1^-	6376	6073	5 4 0 3 ⊗ 2 10 0 0	4	74.49	6539	5 4 0 3 ⊗ 2 10 0 0	4	31.26
			5 3 1 3 ⊗ 2 10 0 0	4	14.55		4 4 1 3 ⊗ 2 10 0 0	4	20.56
10_2^-	6721	6799	5 4 0 3 ⊗ 2 10 0 0	4	47.07	6800	5 3 1 3 ⊗ 2 10 0 0	6	37.61
			4 4 1 3 ⊗ 2 10 0 0	4	19.40		4 4 1 3 ⊗ 2 10 0 0	4	10.78
11_1^-	6954	6561	5 4 0 3 ⊗ 2 10 0 0	4	69.58	6634	4 4 1 3 ⊗ 2 10 0 0	4	33.02
			5 3 1 3 ⊗ 2 10 0 0	6	14.42		5 4 0 3 ⊗ 2 10 0 0	4	17.60
11_2^-	7009	6991	4 4 1 3 ⊗ 2 10 0 0	4	35.76	7147	5 3 1 3 ⊗ 2 10 0 0	6	31.19
			5 4 0 3 ⊗ 2 10 0 0	4	24.91		5 4 0 3 ⊗ 2 10 0 0	4	17.75
15_1^-	8958	9112	4 4 1 3 ⊗ 2 10 0 0	6	52.52	8998	4 4 1 3 ⊗ 2 10 0 0	6	39.89
			5 3 1 3 ⊗ 2 10 0 0	6	29.21		5 3 1 3 ⊗ 2 10 0 0	6	31.59
16_1^-	(9707)	13367	4 3 0 5 ⊗ 2 10 0 0	8	55.59	10273	5 4 0 3 ⊗ 2 9 0 1	6	60.04
			4 2 1 5 ⊗ 2 10 0 0	8	19.80		5 3 1 3 ⊗ 2 9 0 1	6	13.34

presented in Table 1, two sets of calculations predict that the above states are predominated by the $\pi(fp)^{-2}(1g_{9/2})^2$ configurations, including the proton excitations from the completely filled $2p_{1/2}$ orbital into the $1g_{9/2}$ orbital, and the angular momentum of the 8_1^+ state arises from the full alignment of two $1g_{9/2}$ protons. With an increase in the excitation energy, the higher 8_2^+ and 9_1^+ states are primarily dominated by the coupling of two proton holes in *fp* orbitals and two unpaired proton particles in the $1g_{9/2}$ orbital, namely $\pi(1f_{5/2})^{-1}(2p_{1/2})^{-1}(1g_{9/2})^2$ configurations. As presented in Table 1, both SM1 and SM2 calculations give the same results for the 9_2^+ and 10_1^+ states, with $\pi(fp)^{-2}(1g_{9/2})^2$ configurations. It should be noted that the 1575, 1658, 2203, and 2055 keV rays are de-excited from the observed (8^+), 9^+, (9^+), and 10^+ states, respectively. In the neighboring isotone ^{92}Mo [9], the presence of high-energy transitions of approximately 2 MeV at the levels $I = 8 \sim 10\hbar$ is suggested as an experimental indication of nucleons across the $Z = 38$ subshell, which supports the interpretation of excitations across the $Z = 38$ subshell for the aforementioned states in the ^{90}Zr nucleus. SM2 predicts that the 10_2^+ state is mainly dominated by the excitations of two $2p_{1/2}$ and $1f_{5/2}$ protons across the $Z = 40$ and 38 closed subshells into the high-j $1g_{9/2}$ orbital. As presented in Fig. 1, the energy difference between the predicted 11_1^+ and 9_1^+ states of SM2 is 1133 keV, which is close to the energy of the observed 1032 γ ray. The shell model calculations indicate that the 11_1^+ state mainly decays to the 9_1^+ state by the transition with $E2$ multipolarity. Thus, the observed first (11^+) state may correspond to the predicted 11_1^+ state with an energy of 6123 keV obtained from the SM2 calculations, which is also consistent with the temporary spin-parity assignment suggested in Ref. [23]. It is predicted that the 11_1^+ state has the same configuration as the 9_1^+ state, i.e., the $\pi(1f_{5/2})^{-1}(2p_{1/2})^{-1}(1g_{9/2})^2$ configuration, mixed with $\pi(1f_{5/2})^{-1}(2p_{3/2})^{-1}(1g_{9/2})^2$ configuration. For the 12_1^+ state, it has the same $\pi(fp)^{-4}(1g_{9/2})^4$ configuration as the 10_2^+ state.

In Table 1, it can be observed that the primary contribution to the positive-parity states from the 2_1^+ state to the 8_1^+ state comes from the $2p_{1/2}$ proton excitations. For the states from 8_2^+ to the 12_1^+ state, the proton excitations of $1f_{5/2}$ begin to participate in the contribution of the angular momentum. In general, the states from the 0_1^+ ground

state to the 12^+_1 state (0 ~ 7000 keV), are reproduced satisfactorily in both SM1 and SM2. However, for the states above the 12^+_1 state, the values for the excitation energies, calculated within the two different configuration spaces (SM1 and SM2), exhibit significant differences.

It can be seen from Fig. 1 that the predicted energies of the 11^+_2 and 12^+_2 states in SM2, which involve neutron core excitations, are more reasonable than those in SM1. Within SM2 calculations, the observed 11^+_2 and 12^+_2 states could be interpreted as $\pi(fp)^{-2}(1g_{9/2})^2\otimes\nu(1g_{9/2})^{-1}(2d_{5/2})^1$ configurations with seniority $v = 4$, including the coupling of two unpaired $1g_{9/2}$ protons and one $1g_{9/2}$ neutron hole as well as a single $2d_{5/2}$ neutron located above $N = 50$ core, while both states are assigned to the $\pi(fp)^{-4}(1g_{9/2})^4$ configurations in SM1 calculations. It should be noted that the order of levels 11^+_2 and 12^+_2 is opposite in SM2 and is normal in SM1 compared to the data. Considering the differences in configurations obtained by SM1 and SM2, the inverse order of levels 11^+_2 and 12^+_2 given by SM2 may be attributed to the influence of the neutron-proton interaction [45], as an additional neutron is excited to the $2d_{5/2}$ orbital. Furthermore, the excitation energies for the observed 11^+_2 and 12^+_2 states are very close to each other (about 30 keV), and the predicted energy difference between the both states in SM2 is only 10 keV. Such a small energy difference is significantly sensitive to change of configuration space, which is also likely to affect the order of levels in the shell model calculations. In addition, the presence of high-energy 1550 and 1580 keV transitions decaying from the second (11^+) and (12^+) states may be an experimental indication of the $N = 50$ core breaking. Similar features are also observed in ^{91}Nb [8], ^{92}Mo [9], ^{94}Ru [11, 17], and ^{96,97,98}Ru [46]. For example, in the neighboring $N = 50$ isotone ^{94}Ru, the initial states of the high-energy 2200, 2402, 2584, and 2565 keV transitions, namely 13^-_3, 13^-_4, 14^-_1, and 15^-_1 states, respectively, also involve the breaking of the $N = 50$ core.

The improved description for the 11^+_2 and 12^+_2 states in SM2 indicates that the neutron core excitations may play a significant role in the higher-spin states of ^{90}Zr. It is clear from Fig. 1 and Table 1 that within SM2 calculations, the observed (13^+) and (14^+) states may correspond to the calculated 13^+_1 and 14^+_1 states, with the $\pi(fp)^{-2}(1g_{9/2})^2\otimes\nu(1g_{9/2})^{-1}(2d_{5/2})^1$ configurations contributing maximally. In addition, the energy difference between the calculated 13^+_1 and 14^+_1 states is 696 keV, which is close to the energy of the observed 621 keV γ ray [23]. Nevertheless, in SM1 calculations, the predicted excitation energies of 13^+_1 and 14^+_1 states are 1453 and 811 keV higher than the experimental values, respectively, and the order of these two states is inverted. As can be deduced from Fig. 1, the calculated 15^+_1, 16^+_1, 17^+_1, and 18^+_1 states of SM2 may correspond to the experimental levels at 9836, 10126, 10765, and 11404 keV, respectively. The deviations between predicted excitation energies and experimental ones are less than 280 keV, whereas using the SM1 configuration space leads to relatively large differences of 1.0 ~ 2.0 MeV. Within SM2 calculations, the aforementioned states are predominated by $\pi(1f_{5/2})^{-1}(2p_{1/2})^{-1}(1g_{9/2})^2\otimes\nu(1g_{9/2})^{-1}(2d_{5/2})^1$ configurations with seniority $v = 6$, including the excitation of a single $1g_{9/2}$ neutron across the $N = 50$ core into the $2d_{5/2}$ orbital. This further indicates that the contribution from the particle-hole excitations across the $N = 50$ inert core cannot be ignored. The observed (19^+) state with an energy of 12111 keV may correspond to the calculated 19^+_1 state of SM2 at an energy of 12416 keV. Although it has the same proton configuration as that of the 18^+_1 state, it involves neutron excitations across the $N = 50$ core into the $1g_{7/2}$ orbital, i.e., the $\pi(1f_{5/2})^{-1}(2p_{1/2})^{-1}(1g_{9/2})^2\otimes\nu(1g_{9/2})^{-1}(1g_{7/2})^1$ configuration. However, in the SM1 configuration space, the predicted 19^+ is significantly higher than the experimental one, with a difference of more than 10 MeV. In general, it can be inferred from Fig. 1 that the predicted energies of higher-spin states within the SM2 configuration space are more logical than those in SM1.

A similar situation also emerges in the negative-parity states of ^{90}Zr. As can be seen from Fig. 1, the calculations within SM2 containing neutron core excitations provide an improved description for higher-spin states in comparison with the SM1. Hence, the breaking of the $N = 50$ core plays an important role in the higher-spin states of ^{90}Zr, for positive-parity states as well as negative-parity states. The calculated 16^-_1 state primarily originates from the configuration of $\pi(fp)^{-3}(1g_{9/2})^3\otimes\nu(1g_{9/2})^{-1}(2d_{5/2})^1$ with $v = 6$. For the other negative-parity states of ^{90}Zr, the predicted excitation energies within SM1 and SM2 configuration spaces are in logical agreement with the experimental ones. The observed state with an energy of 8958 keV, corresponding to the predicted 15^-_1 state at an energy of 8998 keV, could be interpreted as the configuration of $\pi(1f_{5/2})^{-2}(2p_{1/2})^{-1}(1g_{9/2})^3$, involving the excitations of two $1f_{5/2}$ proton holes across the $Z = 38$ subshell. The 10^-_2 and 11^-_2 states have the same configurations, i.e., $\pi(1f_{5/2})^{-1}(2p_{3/2})^{-1}(2p_{1/2})^{-1}(1g_{9/2})^3$. For the 10^-_1 state, it mainly arises from the coupling of one $1f_{5/2}$ proton hole and three $1g_{9/2}$ proton particles. The 3^-_1 state could be described as the $\pi(2p_{3/2})^{-1}(1g_{9/2})^1$ configuration, with seniority $v = 2$. The calculated wave functions of 4^-_1 and 5^-_1 states indicate a multiplet character, with the predominated $\pi(2p_{1/2})^{-1}(1g_{9/2})^1$ configuration.

B. Evolution from the neutron core excitations to proton excitations

The core excitations are systematically observed in $N = 50$ isotones, generally for the higher-spin states.

However, we note that some specific lower-spin states also include the breaking of the $N = 50$ core. To further understand the core breaking of the lower-spin states, the systematic study of the states for the $N = 50$ even-even isotones ^{86}Kr [47], ^{88}Sr [6], ^{90}Zr [23, 48], ^{92}Mo [9], ^{94}Ru [11], and odd-A isotones ^{85}Br [49], ^{87}Rb [50], ^{89}Y [7], ^{91}Nb [8], ^{93}Tc [10], is presented in Figs. 2(a) and 2(b), respectively, where the states, including the neutron core excitations, are marked in red.

In Fig. 2(a), the 6_1^+ and 7_1^+ states of ^{86}Kr [47] and ^{88}Sr [6] are predominated by the $\nu(1g_{9/2})^{-1}(2d_{5/2})^1$ configurations, associated with the breaking of the $N = 50$ core. Conversely, in ^{90}Zr, the 6_1^+ and 7_1^+ states mainly arise from the proton configurations $\pi(fp)^{-2}(1g_{9/2})^2$. In the heavier ^{92}Mo and ^{94}Ru nuclei, the 6_1^+ and 7_1^+ states are also mainly dominated by the coupling of the two unpaired $1g_{9/2}$ protons, without neutron core excitations.

This indicates an evolution from the neutron core excitations to proton excitations for low-lying states, along the $N = 50$ even-even isotones. This phenomenon appears to be related to the change in the proton Fermi surface. With the decrease in the proton number from ^{90}Zr to ^{86}Kr, the proton Fermi surface moves away from the $1g_{9/2}$ orbital, i.e., the proton excitations from the fp orbitals into the $1g_{9/2}$ orbital become more difficult. In fact, it can be deduced from Fig. 2(a) that for the yrast 6^+ and 7^+ states, the neutron core excitations seem to be more favored than proton excitations. In contrast, as the protons increase from ^{90}Zr to ^{94}Ru, the proton excitations become relatively easy.

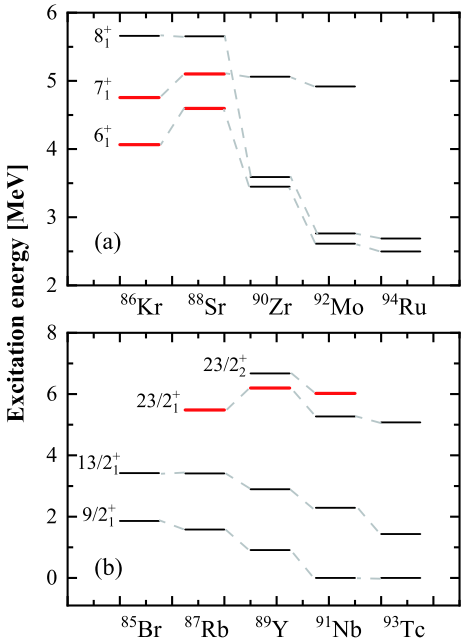

Fig. 2. (color online) Excitation energies for the low-lying states in the $N = 50$ (a) even-even isotones ^{86}Kr [47], ^{88}Sr [6], ^{90}Zr [23, 48], ^{92}Mo [9], and ^{94}Ru [11], and (b) odd-A isotones ^{85}Br [49], ^{87}Rb [50], ^{89}Y [7], ^{91}Nb [8], and ^{93}Tc [10]. The states including the neutron excitations across the $N = 50$ core are marked in red.

A similar situation also emerges at the $23/2^+$ states in the $N = 50$ odd-A isotones. From Fig. 2(b), the yrast $23/2^+$ states of ^{87}Rb [50] and ^{89}Y [7] nuclei, with $Z < 40$, are dominated by the neutron core excitations. The yrast $23/2^+$ states of the ^{91}Nb [8] and ^{93}Tc [10] nuclei, with $Z > 40$, are generated by the proton excitations instead of the neutron core excitations, whereas the yrare $23/2^+$ state of ^{91}Nb includes the neutron core excitation. In particular, the ^{90}Zr nucleus with $Z = 40$, of which the proton Fermi surface lies at the $2p_{1/2}$ orbital, may be a critical nucleus for the structural evolution along the $N = 50$ isotones.

In addition, for the 8_1^+ states with $\pi(1g_{9/2})^2$ configurations in even-even nuclei, the excitation energies decrease with increasing proton numbers, as illustrated in Fig. 2(a). Similarly, in Fig. 2(b), the excitation energies of the $9/2_1^+$ and $13/2_1^+$ states in the odd-A nuclei also exhibit a decreasing character. The behavior of the aforementioned excitation energies also indicates the influence of the change in the proton Fermi surface.

C. Possible magnetic rotation

In Fig. 1, the positive-parity sequence 1 primarily comprises relatively strong $M1$ transitions with absent $E2$ crossover transitions. To further interpret this sequence, the observed spins I are presented in Fig. 3(a) as a function of the rotational frequency $\hbar\omega$, where $\hbar\omega(I) = [E(I) - E(I-2)]/2$. In Fig. 3(a), a sudden backbend occurs at $\hbar\omega \approx 1.2$ MeV, owing to the alignment of the two fp proton holes, which agrees well with the shell model prediction. Based on SM2 calculations, we suggest that the sequence 1 of ^{90}Zr has the $\pi(fp)^{-2}(1g_{9/2})^2 \otimes \nu(1g_{9/2})^{-1}(2d_{5/2}/1g_{7/2})^1$ configuration before the sharp backbend.

In this mass region, the high-j particles and holes are known to play active roles in the magnetic rotation [35]. In fact, these basic conditions for the occurrence of magnetic rotation can be satisfied in the positive-parity sequence 1. Hence, it is interesting to investigate whether sequence 1 emerges from magnetic rotation. Accordingly, the dynamic moment of inertia $J^{(2)}$ of sequence 1 in ^{90}Zr and those of the magnetic rotational bands in the neighboring ^{83}Kr [38], ^{84}Rb [35, 36], and ^{85}Sr [41] nuclei are presented in Fig. 3(b), where $J^{(2)}$ of sequence 1 is similar to those of magnetic rotational bands in the neighboring nuclei. Another typical characteristic of magnetic rotation is the decrease in $B(M1)$ values with increasing spin. The $B(M1)$ values for sequence 1 in nucleus ^{90}Zr [23] and magnetic rotational bands in ^{83}Kr [51], ^{84}Rb [36], and ^{85}Sr [42], are plotted in Fig. 4. As illustrated in Fig. 4, the $B(M1)$ values of ^{90}Zr exhibit a decreasing tendency with increasing spin up to $I^\pi = 14^+$, similar to magnetic rota-

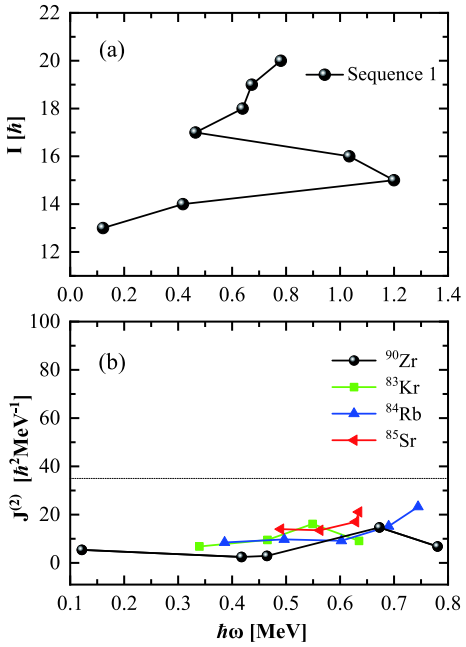

Fig. 3. (color online) (a) Angular momentum as a function of rotational frequency $\hbar\omega$ for sequence 1 in nucleus ^{90}Zr. (b) Comparative dynamic moment of inertia J^2 versus $\hbar\omega$ plot for the magnetic rotational bands in ^{83}Kr [51], ^{84}Rb [36], and ^{85}Sr [41], with the $M1$ sequence in ^{90}Zr. The dash line indicates the value for the rigid spherical rotor.

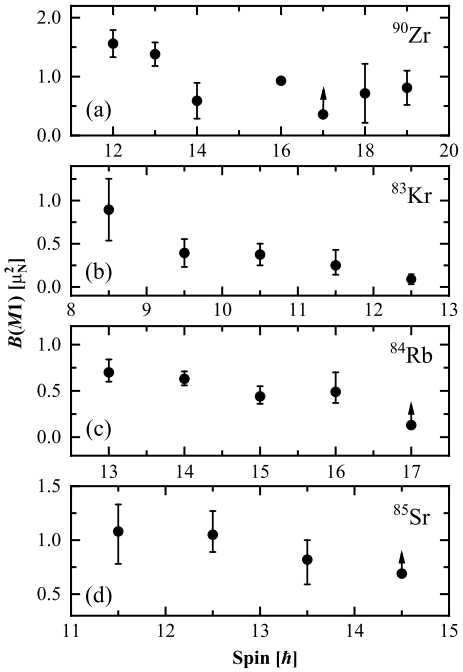

Fig. 4. Comparison of transition rates $B(M1)$ for sequence 1 of nucleus (a) ^{90}Zr [23] and $B(M1)$ values for magnetic rotational bands in (b) ^{83}Kr [51], (c) ^{84}Rb [36], and (d) ^{85}Sr [42] nuclei.

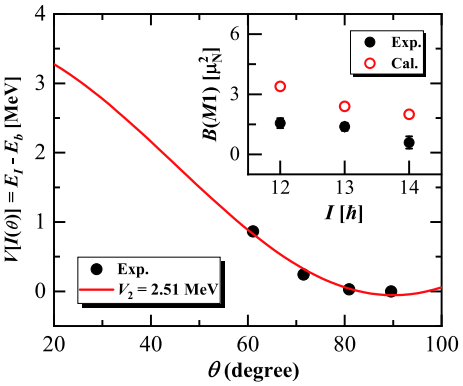

Fig. 5. (color online) Effective interaction as a function of shears angle. The solid curve represents the fit to the experimental data for V_2 = 2.51 MeV. The insert presents the experimental and calculated $B(M1)$ values of the candidate magnetic rotational band in ^{90}Zr.

tional bands of ^{83}Kr, ^{84}Rb, and ^{85}Sr. Meanwhile, the $B(M1)$ values of these nuclei are close to each other, approximately 1.0 μ_N^2. Hence, we suggest that the positive-parity sequence 1 of ^{90}Zr before the backbend ($\sim 14^+$) may also be a candidate magnetic rotational band.

In order to examine the conjecture of magnetic rotation, the theoretical reduced transition probabilities $B(M1)$ for sequence 1 before the backbend are presented as a function of the rotational frequency based on the large scale shell model calculations in the insert of Fig. 5, where the calculated $B(M1)$ values are large (about several μ_N^2) and exhibit a smooth decreasing trend with the increasing spin, which is consistent with the characteristic of magnetic rotation.

To further elucidate the shears mechanism, we perform the semiclassical calculations proposed by A. O. Macchiavelli and R. M. Clark *et al*. [31-34], based on a schematic model with the objective of extracting information on the effective interaction. The calculated energies of sequence 1 are presented as a function of shears angle θ, in comparison with the available data, as illustrated in Fig. 5, where the shears angle decreases gradually with spin increasing. In addition, the data are logically reproduced for V_2 = 2.51 MeV before the band crossing. Meanwhile, we estimate that the interaction strength per proton/neutron-hole pair is $\sim$840 keV for ^{90}Zr, which is close to the value $\sim$900keV adopted for the magnetic rotational band in the neighboring ^{84}Rb [34]. Primarily, the positive-parity sequence 1 of ^{90}Zr before the backbend may originate from the shears mechanism.

IV. SUMMARY

Large scale shell model calculations were performed for ^{90}Zr based on two different configuration spaces. Although SM1 calculations reproduce the lower-spin states well, they fail to logically describe higher-spin states. In contrast to SM1, the SM2 configuration space, including the neutron core excitations, provides an improved de-

scription of the higher-spin states. The SM2 calculations predict that the higher-spin states of ^{90}Zr can be predominated by (i) proton excitations from the *fp* orbitals across the $Z = 38$ or 40 subshell into the higher orbitals, and (ii) neutron excitations from the interior of the $N = 50$ core to the next major shell. This indicates that the neutron core excitations play a significant role in the higher-spin states of ^{90}Zr. Meanwhile, the evolution from the neutron core excitations to proton excitations was systematically studied along the neighboring $N = 50$ isotones for lower-spin states, and ^{90}Zr may be the critical nucleus for the evolution. Furthermore, based on lifetime measurements and characteristics of sequence 1, the positive-parity $\Delta I = 1$ of sequence 1 before the backbend is proposed as a candidate magnetic rotational band with the $\pi(fp)^{-2}(1g_{9/2})^{2}\otimes \nu(1g_{9/2})^{-1}(2d_{5/2}/1g_{7/2})^{1}$ configuration.

References

[1] Y. Zheng, G. de France, X. H. Zhou *et al.*, Chin. Phys. C **44**, 024002 (2020)
[2] S. Saha, R. Palit, J. Sethi *et al.*, Phys. Rev. C **86**, 034315 (2012)
[3] Y. H. Wu, K. Y. Ma, F. Cheng *et al.*, Pramana **94**, 53 (2020)
[4] Y. H. Zhang, M. Hasegawa, W. T. Guo *et al.*, Phys. Rev. C **79**, 044316 (2009)
[5] H. Wang, K. Y. Ma, Y. H. Wu *et al.*, Chin. Phys. C **45**, 014001 (2021)
[6] E. A. Stefanova, R. Schwengner, J. Reif *et al.*, Phys. Rev. C **62**, 054314 (2000)
[7] Z. Q. Li, S. Y. Wang, C. Y. Niu *et al.*, Phys. Rev. C **94**, 014315 (2016)
[8] P. W. Luo, X. G. Wu, H. B. Sun *et al.*, Phys. Rev. C **89**, 034318 (2014)
[9] N. S. Pattabiraman, S. N. Chintalapudi, S. S. Ghugre *et al.*, Phys. Rev. C **65**, 044324 (2002)
[10] M. Hausmann, A. Jungclaus, E. Galindo *et al.*, Phys. Rev. C **68**, 024309 (2003)
[11] A. Jungclaus, D. Kast, K. P. Lieb *et al.*, Phys. Rev. C **60**, 014309 (1999)
[12] T. Back, C. Qi, B. Cederwall *et al.*, Phys. Rev. C **87**, 031306 (2013)
[13] A. Jungclaus, D. Kast, K. R. Lieb *et al.*, Nucl. Phys. A **637**, 346 (1998)
[14] A. Ertoprak, C. Qi, B. Cederwall *et al.*, Eur. Phys. J. A **56**, 291 (2020)
[15] A. Ertoprak, B. Cederwall, C. Qi *et al.*, Eur. Phys. J. A **54**, 145 (2018)
[16] F. G. Moradi, B. Cederwall, C. Qi *et al.*, Phys. Rev. C **89**, 044310 (2014)
[17] F. G. Moradi, C. Qi, B. Cederwall *et al.*, Phys. Rev. C **89**, 014301 (2014)
[18] M. Palacz, J. Nyberg, H. Grawe *et al.*, Phys. Rev. C **86**, 014318 (2012)
[19] E. A. Stefanova, T. Kutsarova, I. Deloncle *et al.*, Nucl. Phys. A **669**, 14 (2000)
[20] S. S. Ghugre and S. K. Datta, Phys. Rev. C **52**, 1881 (1995)
[21] H. A. Roth, S. E. Arnell, D. Foltescu *et al.*, Phys. Rev. C **50**, 1330 (1994)
[22] P. C. Li and W. W. Daehnick, Nucl. Phys. A **462**, 26 (1987)
[23] E. K. Warburton, J. W. Olness, C. J. Lister *et al.*, Phys. Rev. C **31**, 1184 (1985)
[24] H. C. Chiang, M. C. Wang, and C. S. Han, J. Phys. G **6**, 345 (1980)
[25] J. A. Becker, S. D. Bloom, and E. K. Warburton, Amer. Chem. Soc. Symposium Ser. **324**, 78 (1986)
[26] P. E. Garrett, W. Younes, J. A. Becker *et al.*, Phys. Rev. C **68**, 024312 (2003)
[27] J. Meng, J. Peng, S. Q. Zhang *et al.*, Front. Phys. **8**, 1 (2013)
[28] J. Peng, J. Meng, P. Ring *et al.*, Phys. Rev. C **78**, 024313 (2008)
[29] P. W. Zhao, S. Q. Zhang, J. Peng *et al.*, Phys. Lett. B **699**, 3 (2011)
[30] Y. K. Wang, Phys. Rev. C **97**, 064321 (2018)
[31] A. O. Macchiavelli, R. M. Clark, P. Fallon *et al.*, Phys. Rev. C **57**, R1073 (1998)
[32] A. O. Macchiavelli, R. M. Clark, M. A. Deleplanque *et al.*, Phys. Rev. C **58**, R621 (1998)
[33] R. M. Clark, S. J. Asztalos, B. Busse *et al.*, Phys. Rev. Lett. **82**, 3220 (1999)
[34] R. M. Clark and A. O. Macchiavelli, Ann. Rev. Nucl. Part. Sci. **50**, 1 (2000)
[35] H. Schnare, R. Schwengner, S. Frauendorf *et al.*, Phys. Rev. Lett. **82**, 4408 (1999)
[36] R. Schwengner, G. Rainovski, H. Schnare *et al.*, Phys. Rev. C **66**, 024310 (2002)
[37] R. Schwengner, F. Donau, T. Servene *et al.*, Phys. Rev. C **65**, 044326 (2002)
[38] S. S. Malik, P. Agarwal, and A. K. Jain, Nucl. Phys. A **732**, 13 (2004)
[39] Amita, A. K. Jain, V. I. Dimitrov *et al.*, Phys. Rev. C **64**, 034308 (2001)
[40] S. Ganguly, P. Banerjee, I. Ray *et al.*, Nucl. Phys. A **768**, 43 (2006)
[41] S. Kumar, N. Kumar, S. Mandal *et al.*, Phys. Rev. C **90**, 024315 (2014)
[42] N. Kumar, S. Kumar, S. K. Mandal *et al.*, Eur. Phys. J. A **53**, 25 (2017)
[43] B. A. Brown and W. D. M. Rae, Nucl. Data Sheets **120**, 115 (2014)
[44] Y. Zheng, Y. H. Wu, X. G. Wu *et al.*, Phys. Rev. C **100**, 014325 (2019)
[45] M. Hasegawa, Y. Sun, S. Tazaki *et al.*, Phys. Lett. B **696**, 197 (2011)
[46] B. Kharraja, S. S. Ghugre, U. Garg *et al.*, Phys. Rev. C **57**, 83 (1998)
[47] G. Winter, R. Schwengner, J. Reif *et al.*, Phys. Rev. C **48**, 1010 (1993)
[48] H. Fann, J. P. Schiffer, and U. Strohbusch, Phys. Lett. B **44**, 19 (1973)
[49] R. J. Guo, Z. Q. Li, C. Liu *et al.*, Chin. Phys. C **41**, 084105 (2017)
[50] Y. H. Zhang, Zs. Podolyàk, G. de Angelis *et al.*, Phys. Rev. C **70**, 024301 (2004)
[51] P. Kemnitz, J. Doring, L. Funke *et al.*, Nucl. Phys. A **456**, 89 (1986)